Journal of Cleaner Production 246 (2020) 118748

Contents lists available at ScienceDirect

Journal of Cleaner Production

journal homepage: www.elsevier.com/locate/jclepro

Development of a high-temperature inorganic synthetic foam with recycled fly-ash cenospheres for thermal insulation brick manufacturing

Adam L. Brooks [a], Zhenglai Shen [b], Hongyu Zhou [a, *]

[a] Department of Civil and Environmental Engineering, University of Tennessee, Knoxville, 851 Neyland Drive, TN, 37996, USA
[b] Department of Civil and Environmental Engineering, University of Alabama in Huntsville, 5000 Technology Drive, AL, 35899, USA

ARTICLE INFO

Article history:
Received 17 March 2019
Received in revised form
30 August 2019
Accepted 5 October 2019
Available online 10 October 2019

Handling Editor: Zhen Leng

Keywords:
Fly-ash cenosphere
Synthetic foam
Thermal insulation
Thermal modeling

ABSTRACT

In this study, a novel inorganic synthetic solid foam composed of recycled fly-ash cenospheres (FACs) is developed with low-density, good thermal insulation performance, and reasonable mechanical strength. The manufacturing process utilizes low-fraction clay binder materials diluted in water, enabling a self-assembling mechanism assisted by natural capillary effect to form minimal contacts among the FACs. The microstructure and minimal contact formation were confirmed by optical and electron microscope imaging. Both thermal and mechanical properties of the fly-ash cenosphere synthetic solid foam (FAC-SSF) materials were experimentally studied as functions of key material parameters including cenosphere particle size and clay content. A numerical model was developed to predict the effective thermal conductivity of FAC-SSF using a three-step homogenization method which takes into account different thermal percolation paths within the material. The inorganic synthetic foam developed has the potential for thermal insulation applications taking advantage of their relatively simple, low-cost, and scalable manufacturing process, minimal use of binder materials, and relatively high mechanical strength and highly tailorable properties.

1. Introduction

According to the World Coal Institute, power plants fueled by coal produce approximately 41% of global electricity and it is estimated that the importance of coal to electricity generation is set to continue with coal power plants fueling 44% of global electricity by 2030 (Ranjbar and Kuenzel, 2017). The percentage of electricity generated by coal-fueled power plants is even higher for some countries and regions like China and India (Dwivedi and Jain, 2014). As an important by-product of the coal burning process, a tremendous amount of fly ash – a waste material consisting of the non-combustible mineral portion of coal, is produced worldwide (i.e., coal-fired power plants produce over 500 million tons of fly ash each year (Sheikh, 2018)). Fly ash is generally composed of amorphous alumino-silicate with varying amounts of calcium, which when mixed with Portland cement and water, will react with the calcium hydroxide released by the hydration of Portland cement to produce various calcium-silicate hydrates (C–S–H) and calcium-aluminate hydrates (Lam et al., 2000). Some fly ashes with higher amounts of calcium will also display cementitious behavior by reacting with water to produce hydrates in the absence of a source of calcium hydroxide. These pozzolanic reactions are beneficial to concrete by improving the long-term strength and reducing the permeability of concrete materials (Barbhuiya et al., 2009). For these reasons, a large quantity of fly ash waste is used every year by the concrete industry. However, it is clear that, even though millions of tons of coal combustion products are used in concrete production, millions more are still going to waste. According to the American Coal Ash Association (ACAA), in 2017 the United States alone produced 110 million tons of coal combustion products. While 60% were used beneficially, nearly 38 million tons were disposed of (American Coal Ash Association, 2018). Therefore, further applications need to be developed in order to recycle them (Blissett and Rowson, 2012; Siddique, 2010).

Fly ash cenospheres (FAC), or alumino-silicate hollow microspheres, represent one of the microspherical components of sialic

* Corresponding author. 851 Neyland Drive, 417 John D. Tickle Building, Knoxville, TN, 37996-2313, USA.
E-mail addresses: abrook51@vols.utk.edu (A.L. Brooks), zs0006@uah.edu (Z. Shen), hzhou8@utk.edu (H. Zhou).

https://doi.org/10.1016/j.jclepro.2019.118748
0959-6526/

fly ash (Zyrkowski et al., 2016), which are featured by low bulk density (400–900 kg/m^3) and can be easily separated by the gravitational method in the form of a concentrate in aqueous media (Fomenko et al., 2011). The formation of cenospheres occurs as a result of thermochemical and phase transformations of the original mineral coal forms in the course of its combustion. The granulometric, chemical, and phase-mineral compositions of the cenospheres depend on the composition of the original coal, type of furnaces employed, and the conditions for cooling melt droplets etc.(Fomenko et al., 2011). The content of cenospheres in fly ash from the combustion of different types of coals varies over a rather wide range from 0.5 to 4.8 wt % (Zyrkowski et al., 2016). Due to their many beneficial properties, such as low-thermal conductivity and lightweight, FACs are considered as a valued industrial waste byproduct. In recent years, numerous researches have focused on utilizing FACs to prepare porous lightweight composites (Hanif et al., 2017). Cementitious composites and concrete have been made with FACs in order to reduce the density and improve the thermal insulation (Brooks et al., 2018; Zhou and Brooks, 2019). The FACs were also used as a filler and reinforcement in polymer-matrix composites (PMCs) (Deepthi et al., 2010) and metal-matrix composites (MMCs) (Rohatgi et al., 2011). However, the use of FACs in bulk form has been rarely reported.

Meanwhile, the search for materials offering high thermal insulation has attracted increasing attention from the modern construction and building industry, since the energy-efficiency of buildings and industrial facilities has become of ever increasing concern (Biswas et al., 2016). Due to the flammable nature of many types of organic insulation materials and the concern for fire safety in buildings and other industrial facilities, there has been increasing efforts to study inflammable and thermally insulating inorganic materials suitable for construction (Chen et al., 2018; Wi et al., 2019), where foamed concrete and geopolymers are well known examples for their relatively low thermal conductivity, usually 10–50% of that of normal weight concrete, depending on the material density and composition (Shao et al., 2018). This low thermal conductivity brings good thermal insulation, and usually better energy efficiency in operation. However, most foamed concrete and geopolymer produced to date has relatively poor mechanical properties (e.g., compressive strength < 4 MPa), which prohibit their use in applications requiring structural integrity such as refractory linings and thermal insulation for industrial facilities including waste incinerators and blast furnaces (Sadik et al., 2014). Moreover, cementitious and geopolymer based materials are known to be susceptible to excessive dry shrinkage and associated cracking, as well as chemical attacks, e.g., sulfate, which limit their use in industrial processing facilities and harsh environments (Bernal and Provis, 2014; Chindaprasirt et al., 2004).

In order to circumvent the drawbacks of conventional insulation materials mentioned above, this paper reports the development of an innovative inorganic solid foam material made from recycled fly ash cenosphere materials. The material, referred herein to as 'Fly-Ash Cenosphere Synthetic Solid Foam' (FAC-SSF), is produced by mixing polydispersed FAC hollow particles into a diluted clay-water suspension. During the drying process, capillary effect (surface tension) will preferentially precipitate the clay particles at the FACs junction points. Then, the inorganic solid synthetic foam is formed by sintering the dried FAC-clay mixture under high temperature. The mechanical and thermophysical properties of FAC-SSF are studied as functions of FAC particle size (type) and the volume fraction of clay binder. The developed FAC-SSF material is low-cost and can be produced for high volume applications – such as fire-resistant insulation, high temperature thermal barriers for industrial applications, refractory linings, as well as 'thermal breaks' in buildings to reduce thermal bridging.

2. Development of the solid synthetic foam using fly-ash cenospheres

In this study, fly-ash cenosphere synthetic solid foams (FAC-SSF) are developed using two types of FACs with different particle size distributions – ES106 (Cenostar) has particle size up to 106 μm, and ES200/600 (Cenostar) has particle size mostly between 200 and 600 μm, see Fig. 1 (a). X-ray Diffraction (XRD) analysis performed on the FACs (Fig. 1 (d)) indicated that the FACs are comprised mostly of silica-based amorphous materials with small amounts of mullite and calcite. The ES200/600 also contains a small amount of quartz. The particle shell thicknesses were measured using scanning electron microscopy (SEM) imaging where the particles were embedded in epoxy and grinded using a Buehler EcoMet™ grinder/polisher to expose the section of the FAC shell. Fig. 1 (b) and (c) presents the SEM images showing the surface morphology and exposed cross section of the FACs. ES106 and ES200/600 have densities (tested by gas pycnometry) and thermal conductivities (densely compacted bulk material tested using Transient Plane Source (TPS) method) of 0.91 g/cm^3 and 0.129 W/mK for ES106, and 0.82 g/cm^3 and 0.138 W/mK for ES200/600, respectively. A non-calcareous illitic clay was used as the binding medium for the solid synthetic foam. Fig. 1 (d) shows the X-ray diffraction (XRD) results of both the unfired and fired clay binder used in this study. The unfired clay contains kaolinite, illite, quartz, and albite, while after being sintered at 1050 °C the clay ceramic contains quartz, haematite, spinel, and albite. The density of the sintered clay was tested at 2014 kg/m^3 with a thermal conductivity tested by TPS at 1.022 W/mK, see Table 1.

To prepare the synthetic solid foam, the binding clay was first made into a slurry. The slurry was prepared by mixing moist clay (with an initial water content of 24%) with water at weight ratios ranging from 1:0.5 to 1:2 (moist clay: water), which results in a final water content of 1.00, 1.12, 1.46, 2.73, and 5.25. The various water contents were designed to make FAC-SSF with different filler (FAC)/binder (clay) ratio – i.e., water content is adjusted to ensure consistent workability of the FAC-clay slurry mixture. The FACs were then mixed with the clay slurry using a planetary mixer to form a composite paste, see Fig. 2 (a). Note that relative volume fractions of FAC, water, and clay particles within the composite paste would dictate the void ratio and the filler to binder ratio of the final sintered FAC-SSF, see Table 2 and Fig. 2. After the desired consistency was reached, the FAC/clay slurry mixture was packed into molds (5.08 cm × 10.16 cm cylinders for mechanical testing and 5.08 cm × 5.08 cm × 5.08 cm cubes for TPS measurements) using a tap rod and a flat-bladed trowel.

The specimens were then air dried for 48 h to help prevent excessive dry shrinkage, before they were placed in a convective oven for 24 h at 110 °C. During the drying process, capillary effect (surface tension between water and the FAC surfaces) causes clay particles to conglomerate at the locations where cenospheres are touching (with some smaller amounts precipitated on FAC surfaces), see Fig. 2 (b). After the samples were oven dried, they were moved to a programmable furnace and sintered at 1050 °C. The sintering process (Fig. 2 (c)) was carried out in three stages: first, the furnace temperature was increased at a rate of 1.0 °C/min until the sintering temperature was reached; then, the temperature was held constant for 5 h before being cooled at a rate of 2.0 °C/min. During the sintering process, the dihydroxylation of illitic clay occurs between 350 °C and 600 °C, where –OH in illite is lost due to heating (McConville and Lee, 2005). At this temperature, carbon and organic matter (if any) were burnt off; at around 675 °C, the small amount of calcite in FACs decomposes to cause noticeable surface color change of the materials. At around this same temperature the original crystal structure of the illite

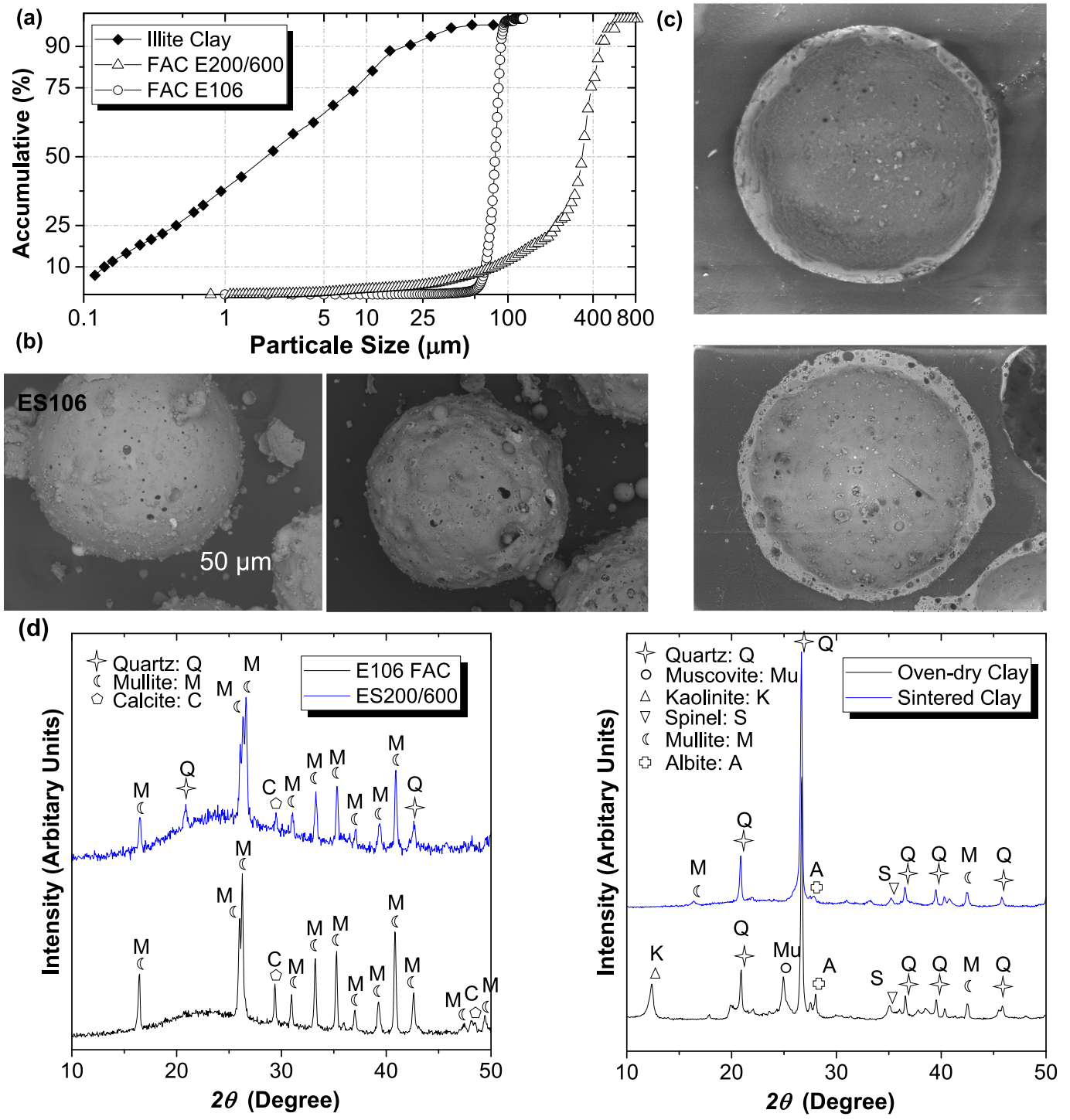

Fig. 1. Properties of fly-ash cenosphere (FAC) and clay used in this study: (a) particle size distribution of FACs and clay particles; (b) surface morphology of the two types of FACs used (i.e., ES106 and ES200/600); (c) polished cross-section of FAC particles showing the shell and empty interior; (d) XRD spectrum for FACs and clay.

begins to break down. Lastly at around 900 °C the illite clay particles begin the transition into its liquid phase and vitrification occurs where clay particles fuse together forming a contiguous, amorphous glassy solid (McConville and Lee, 2005). The optical microscopic image of a final sintered FAC-SSF (ES200/600) is shown in Fig. 2 (c).

3. Experimental program, results, and discussion

3.1. Formation and microstructure of FAC-SSF

In this study, two groups of FAC-SSF were created using two different types of FACs with different particle sizes (ES106 and ES200/600). The two group of specimens made with different FACs

Table 1
Physical properties of FACs and clay used in this study.

Constituent	Particle Size			Density (true)	Density (Bulk)	Thermal Conductivity (Bulk)	Crush strength
	D_{10}	D_{50}	D_{90}				
		um		kg/m^3	kg/m^3	W/mK	MPa
ES106	42.6	81.3	125.2	910	424	0.1285	1.6–3.2
ES200/600	81.3	349.1	457.2	820	395	0.1377	1.2–2.6
Clay (as-is)	0.14	2.18	20.45	2493[a]	1967	–	–
Clay (fired)	–	–	–	2014	–	1.022	12.2

[a] Specific gravity of clay particle used was tested at 2.493 g/cm^3 based on ASTM D854-14.

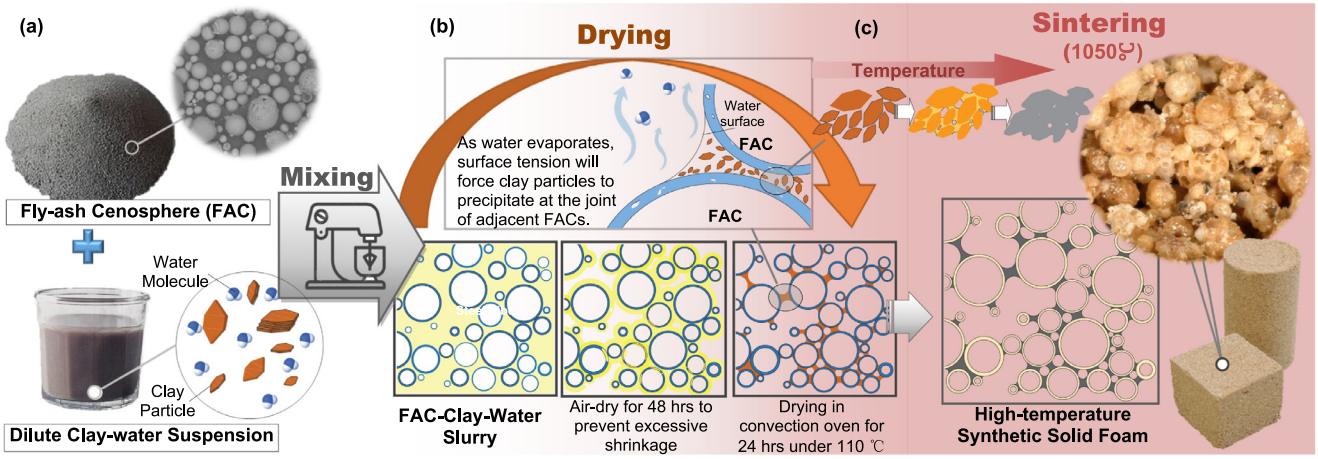

Fig. 2. Illustrative figure showing the process to produce FAC synthetic solid foams (FAC-SSF): (a) preparation of the FAC-clay slurry composite paste; (b) drying; and (c) sintering.

Table 2
Admixtures used to prepare the experimental specimens.

Mix ID	Clay (moist)[a]	FAC	Water (added)	Air in Paste	Volume Fractions				Solid Content	Fired Density
					Clay	FAC	Water	Air[b]		
	g/L	g/L	g/L	cm^3	vol%	vol%	vol%	vol%	vol%	g/cm^3
FAC–SSF–200/600-30	401.2	356.7	205.0	141.4	12.2	43.5	30.1	14.1	29.2	717.8
FAC–SSF–200/600-25	218.9	389.1	133.4	272.8	6.7	47.5	18.6	27.3	25.2	636.9
FAC–SSF–200/600-22	107.1	378.3	108.2	372.1	3.3	46.1	13.4	37.2	21.3	529.9
FAC–SSF–200/600-20	64.4	363.0	118.1	404.1	2.0	44.3	13.4	40.4	19.3	461.4
FAC–SSF–200/600-18	36.4	369.7	136.5	392.9	1.1	45.1	14.5	39.3	18.7	440.7
FAC–SSF–106-30	412.1	392.9	210.6	133.1	12.6	43.2	30.9	13.3	31.3	719.6
FAC–SSF–106-25	213.8	407.6	130.3	305.3	6.5	44.8	18.2	30.5	25.9	612.7
FAC–SSF–106-23	107.6	407.6	108.7	384.7	3.3	44.8	13.5	38.5	22.7	527.3
FAC–SSF–106-20	64.4	389.4	118.1	418.9	2.0	42.8	13.4	41.9	20.5	448.4
FAC–SSF–106-18	36.4	396.5	136.5	408.0	1.1	43.6	14.5	40.8	20.0	423.5

[a] Mixture shown in grams of constituents per unit volume (1000 cm^3) of the wet FAC-clay composite paste.
[b] Air content within wet admixture shown does not include the cavity (interior) within FAC.

were tested to study effects of the FAC particle size on FAC-SSF properties. Each group consisted of five specimen groups with decreasing solid content volume ratio (i.e., FAC shell + the binding clay), see Table 2. The relative amount of moist clay, water (added to form the clay slurry), and FAC were adjusted for each mixture to result in a final solid content within FAC-SSF ranging from 18 to 32%. The five mixtures within each specimen group were designed to study the effects of the clay content, and therefore the total solids content, on the density, mechanical strength, and thermal conductivities of FAC-SSF. The mixtures were also designed to demonstrate the tailorability of the FAC-SSF material in terms of its density, mechanical and thermal properties. The fired densities of FAC-SSF made in this study are in the range of 420–720 kg/m^3 (see Table 2).

It is noted that the objective of this study is to produce FAC syntactic foams with minimal FAC–binder contacts, thereby minimizing thermal transport within the materials. This is realized by the FAC–clay slurry mixtures shown in Tables 2–i.e., high FACs volume fraction mixed with binder (clay) diluted in water – water eventually evaporates during the drying and sintering process (Fig. 2). Fig. 3 presents the optical microscopy images taken by a *Keyence VHX-6000* digital microscope showing the microstructures of two FAC-SSFs formed by the process shown in Fig. 2, i.e., FAC–SSF–200/600–30 and FAC–SSF–200/600–18. It was observed that the FAC–clay binder contact formation sensitively changes depending on the relative volume of clay with respect to the inter-particle void space (i.e., clay vol%/(water vol% + air vol%) listed in Table 2). For FAC–SSF–200/600–30 (Figs. 3 (a), 28% of the

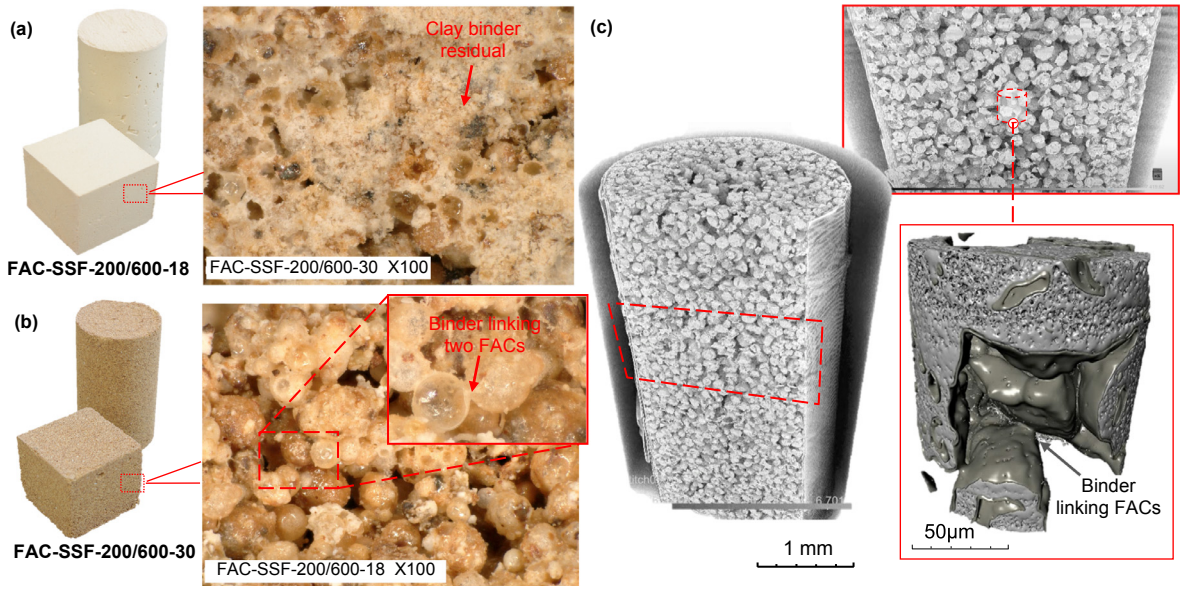

Fig. 3. (a) Optical microscopy images of FAC-SSF with high clay ratio in the inter-particle void space; and (b) low clay ratio (both made with ES200/600 FAC); (c) X-ray microscopy (XRM) results showing the microstructure of the FAC synthetic foam and the clay binder linking the FACs.

inter-particle void space is filled with clay particles) excessive clay binder residues in between the FACs are clearly visible; however, less binder residues are found at a reduced clay-to-void volume ratio – FAC–SSF–200/600–18 with only 2% of inter-particle void space filled by clay shows minimal clay residue selectively located at the FAC junctions, see Fig. 3 (b). The reconstructed microstructure of FAC synthetic foam was shown in Fig. 3 (c) (X-ray microscopy (XRM) scan performed using *Carl Zeiss Versa 520*), where the sintered clay linking adjacent FACs are clearly observed.

The mechanism involved with minimal contact formation between the FACs and clay binder is schematically shown in Fig. 2 (b). Initially, the FACs are well dispersed within a uniformly mixed solution of binder (clay) – water slurry at binder fractions ranging from 7.5% to 40% (vol% of clay particle to water). When the composite paste is dried in a convection oven, water starts to evaporate. Since water is gradually depleted from the paste, the clay-water mixture will densify and precipitate on FAC surfaces and where FACs are in contact with each other in order to minimize surface energy. In the meantime, the process will induce local fluidic motion in such a way that the FACs are attracted to each other. Then, the small void space between FACs attracts the clay binder residues in droplet shape via the capillary effect, preferentially locating the binder at the FACs junction points. The movement of the FACs will gradually slow down as the increased binder concentration (as a result of water evaporation) leads to increased viscosity of the solution. Upon complete removal of free water, curing (solidification) of the binder materials assisted by heating will terminate the minimal contact formation process. It should be noted that the aforementioned process assisted by the surface energy minimization is subject to the amount of clay binder residues; if excessive clay exists in the clay-water solution, the local droplet formation process may not be activated in a favorable way (Miskin and Jaeger, 2012), see Fig. 3 (a).

3.2. Mechanical and thermal test methods

3.2.1. Thermal conductivity measurements by transient plane source (TPS) method

The transient plane source (TPS) method (Gustafsson, 1991) was employed to measure the thermal conductivity of the synthetic foams and cenospheres. The TPS technique is based on the recorded temperature rise of a plane source that heats the surrounding material to be measured. In a TPS test, a conducting pattern with negligible heat capacity (e.g., Kapton supported double spiraled nickel metal sensor as shown in Fig. 4) serves simultaneously as the heat source and the temperature sensor. The initial electrical resistance of the TPS element, R_0, is first balanced in a Wheatstone bridge and, during the measurements, the unbalanced voltage drop is recorded as the function of time using a high-impedance digital voltmeter (Gustafsson, 1991). Through a process of iterations, the thermal conductivity χ and thermal diffusivity κ of the tested material can be simultaneously obtained from one single transient recording (He, 2005). For thermal conductivity measurements, two 50.8 mm cube samples were prepared. The TPS tests were performed using a *HotDisk TPS-1500* analyzer per ISO22007-2 specifications (ISO22007-2:2008, 2008). All samples were dried in a convection oven for 48 h and cooled down to room temperature in an air-tight desiccant cabinet to prevent surface condensation.

3.2.2. Mechanical testing

The mechanical tests were performed using a 50 kN MTS Insight electromechanical universal testing system as shown in Fig. 5 (a). Three 50.8 mm (2 inches) diameter by 101.6 mm (4 inches) cylinders were tested for each specimen group listed in Table 2. The mechanical loading procedure was carried out in a displacement-control mode at the loading rate of 0.01 mm/min. The deformation (i.e., compressive strain) of test cylinders was measured using a pair of clamp-on extensometers (*Epsilon Tech*) with gauge length of 50 mm. The extensometer pair was clamped onto the specimen to measure the strains on both sides of the cylinder. The setup of extensometers is shown in Fig. 5 (b). A high-resolution CCD camera was staged to record the damage and failure of the specimens. The tested specimens were preserved for scanning electron microscopy (SEM) analysis.

3.3. Results and discussion

3.3.1. Thermal and physical properties

The density and thermal conductivity tested for the FAC-SSF are summarized in Table 3. The material density was plotted against

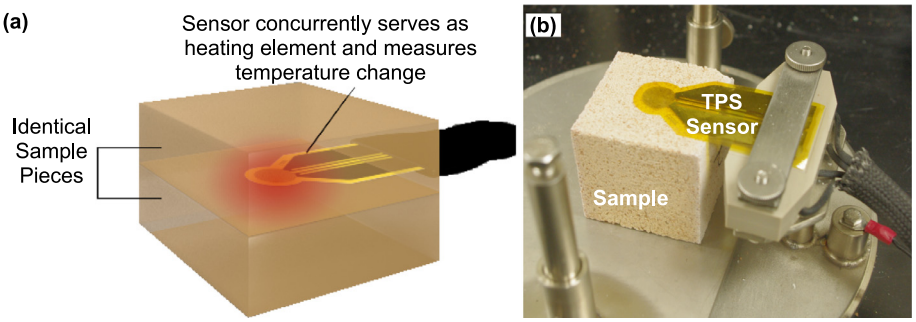

Fig. 4. (a) Illustrative figure and (b) picture showing the Transient Plane Source (TPS) method for thermal property testing.

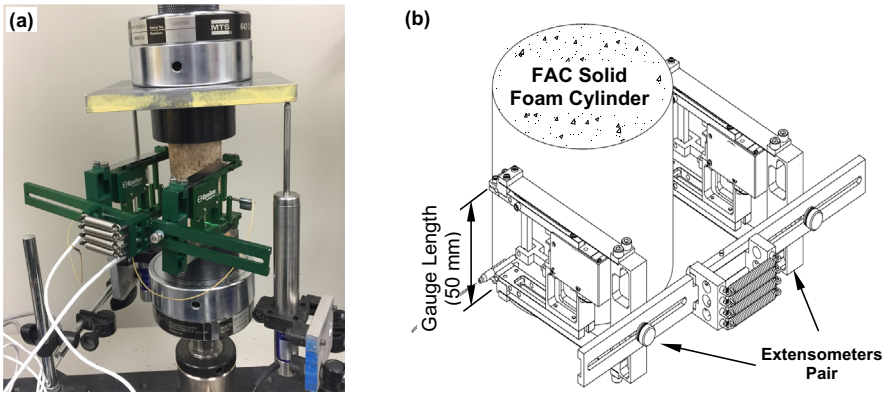

Fig. 5. Mechanical test setup: (a) picture showing the compressive test; and (b) setup of extensometers for Young's modulus measurement.

solid content (the estimated total volume fraction of FAC shell material and clay) in Fig. 6 (a) and the thermal conductivity was plotted against density in Fig. 6 (b). Heat transmission resistance of building components are affected by the thermal conductivity of building materials; specific heat and density, on the other hand, describe building components' ability to store thermal energy and is important to maintain thermal comfort in transient conditions. The thermal conductivity of FAC-SSF is mainly a function of the solid content (Table 2), this is due to the increase of air content in the foam which will reduce the physical pathways for heat transfer, see Fig. 6 (b). Lower clay content in the minimal contact FAC-clay forming process causes the thermally conductive clay particles to selectively conglomerate near the contact points of the FACs, minimizing the conductive pathways within the FAC-SSF material. The thermal conductivity of FAC-SSF decreases almost linearly as the material density reduces. The thermal conductivity of the highest density sample group made in this study was roughly 30% of that of fired clay; whereas the thermal conductivity of lowest density sample is only 15% of that of fired clay. The thermal conductivity reduction is attributed to both the air trapped in the interior cavity of FAC, as well as the connected air voids between FAC particles. Since the air voids between FACs are mostly interconnected, its influences on FAC-SSF thermal conductivity should be treated differently than the air entrapped within FAC's inner core. A more detailed discussion on this phenomenon will be provided later in the modeling section.

During the TPS measurements, the thermal diffusivity of material is concurrently measured with thermal conductivity through an iterative process using the transient heating data (Gustafsson, 1991). Thus, the material's specific heat capacity, c_p, can be calculated based on the thermal diffusivity, κ, materials density, ρ, and thermal conductivity χ via: $c_p = \chi/(\rho\ \kappa)$. The volumetric heat

Table 3
Experimental results[a].

Mix ID	Thermal Conductivity	Volumetric Heat Capacity	Young's Modulus	Compressive Strength
	W/mK	kJ/m^3	GPa	MPa
FAC−SSF−106-30	0.306 ± 0.002	541.5 ± 19.0	5.8 ± 0.212	19.4 ± 1.413
FAC−SSF−106-25	0.251 ± 0.017	493.9 ± 7.9	4.0 ± 0.154	12.8 ± 0.497
FAC−SSF−106-22	0.230 ± 0.004	410.3 ± 5.2	3.2 ± 0.032	9.2 ± 0.420
FAC−SSF−106-20	0.188 ± 0.003	454.5 ± 1.1	2.2 ± 0.074	4.7 ± 0.273
FAC−SSF−106-18	0.173 ± 0.002	423.7 ± 2.6	1.4 ± 0.023	1.9 ± 0.098
FAC−SSF−200/600-30	0.314 ± 0.013	586.2 ± 14.6	4.2 ± 0.196	13.0 ± 0.014
FAC−SSF−200/600-25	0.249 ± 0.005	551.1 ± 5.2	3.3 ± 0.074	8.4 ± 0.005
FAC−SSF−200/600-22	0.214 ± 0.007	445.9 ± 2.4	2.6 ± 0.166	5.8 ± 0.064
FAC−SSF−200/600-20	0.157 ± 0.004	523.0 ± 4.4	0.9 ± 0.047	1.1 ± 0.075
FAC−SSF−200/600-18	0.161 ± 0.003	491.3 ± 0.95	0.9 ± 0.076	1.0 ± 0.120

[a] Results are presented as the statistical average of measurements on three specimens. The standard deviations are listed and shown as error bars in Figs. 6 and 7.

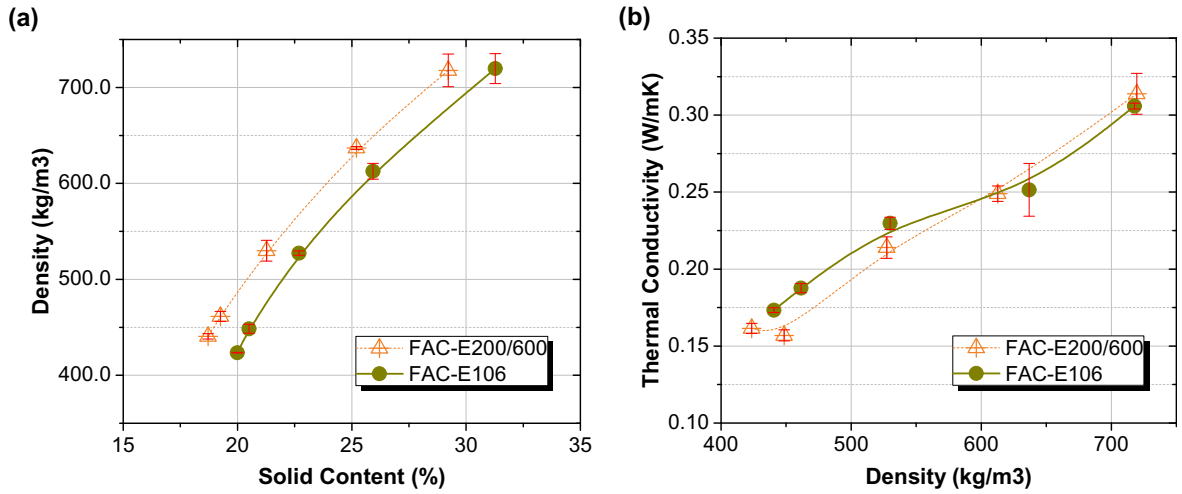

Fig. 6. Thermophysical properties of FAC-SSF showing the relationships between: (a) material density and solid content; and (b) thermal conductivity and density.

capacity tested for FAC-SSF decreases proportionally with the decrease of material density, and is mostly within the range of 420–585 kJ/m^3.

3.3.2. Mechanical properties

The mechanical test results are also summarized in Table 3. Fig. 7 shows Young's Modulus and compressive strength plotted against the materials' density. As the material density increases the compressive strength increases nearly linearly, as does the Young's Modulus. In general, FAC-SSF samples made with ES106 FAC have higher strength and Young's Modulus than those made from ES200/600. This was expected since the smaller particle size of ES106 creates a more densely packed synthetic foam than that of the larger ES200/600 FACs (which have more voids in bulk form). The difference in mechanical property between the two FAC-SSF groups are even higher at high clay content – at lower binder (clay) content, the material's failure is dictated by the strength of the linking element amongst FACs; whereas at high clay content, the strength and stiffness of FAC-SSF is dictated by the stiffness and strength of the FAC particle.

Fig. 8(a) and (b) present the stress-strain behavior of FAC-SSF tested for the two specimen groups made with ES106 FAC and ES200/600 FAC, respectively. It can be seen that smaller FAC particle size (i.e., ES106) generally leads to higher mechanical strength and ductility, especially at higher clay binder content. Since larger size FACs generally have lower crush strength (see Table 1) the FAC-SSF composites made with them also have lower strength as compared to that of FAC-SSF made with smaller size FACs. Additionally, since smaller FAC particle size also leads to much higher surface area (thus, larger contact surfaces between FACs), the FAC-SSFs made with ES106 FAC exhibit better strain ductility, see the comparison from Fig. 8 (a) and (b). Fig. 8 (c) shows the initial failure modes of the highest and lowest clay content for both ES106 and ES200/600, which clearly indicate the dependency of failure modes on clay content – i.e., when the clay binder content is high, the specimens typically fail in shear mode, see Fig. 8 (a) and (c); whereas splitting and local crushing occur more frequently with specimens with lower clay content. When the clay binder content increases, the material's failure mode switches from the breakage of binder links between FACs to the facture of FAC shells. This is evidenced by the SEM images taken on the fracture surfaces of mechanical tested samples (Fig. 9), where the failure of samples with high clay content (Fig. 9 (a) and (c)) present a large number of FAC shells fractured; whereas the samples with low clay content mostly failed at the weak linkage among FACs (thus, most FACs are still intact at the fracture surface), see Fig. 9 (b) and (d).

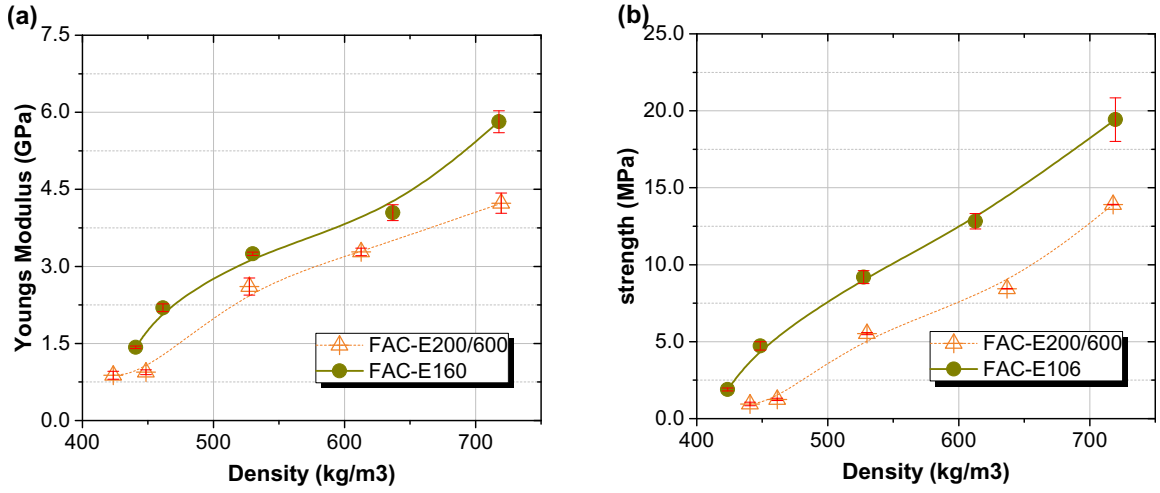

Fig. 7. Relationship between (a) Young's modulus and (b) compressive strength with oven-dry density (error bars indicate the standard deviations of the test results).

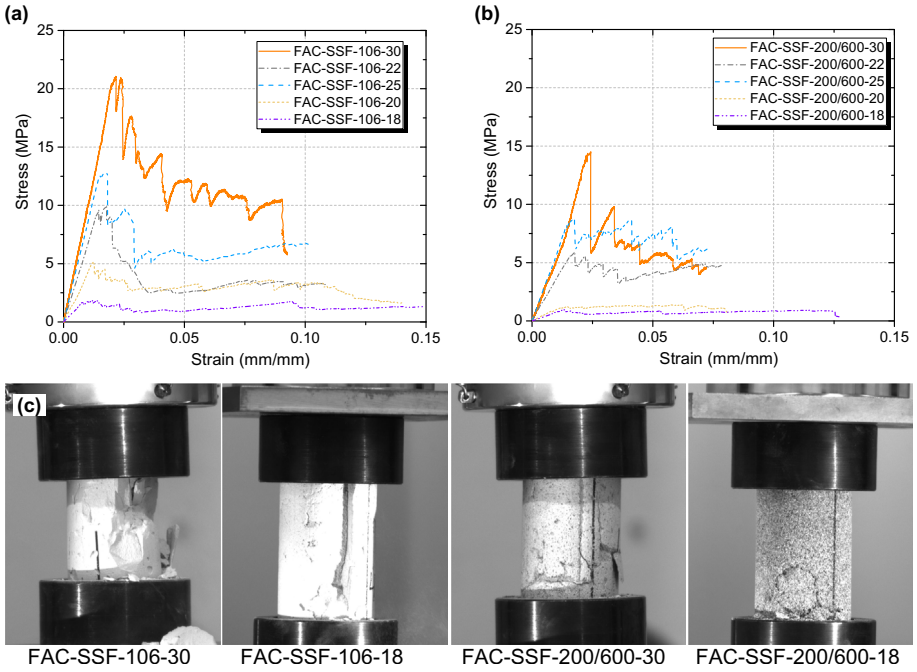

Fig. 8. Mechanical test results: (a) stress-strain results for FAC-SSF made with ES106 FAC; (b) stress-strain results for FAC-SSF made with ES106 FAC; and (c) CCD camera images showing the failure modes of FAC-SSF with different FAC and clay content.

3.3.3. Effects of particle size and clay content

Fig. 10 compares the influence of FAC type and clay content on thermal and mechanical properties of FAC-SSF. The clay content, which indicates how much inter-particle void space is occupied by sintered clay binder, is defined as the ratio between the volume fraction of clay binder, ϕ_c, to the volume fraction of inter-particle void space among FACs, $\phi_c + \phi_{a,\mathrm{IP}}$, where $\phi_{a,\mathrm{IP}}$ is the air volume fraction between FACs, see Fig. 10 (a). For the ten mixtures of FAC-SSF specimens made in this study, the clay ratio ranged from 2% to about 22%. As the clay content increases, effective thermal conductivity of FAC-SSF increases proportionally, see Fig. 10 (b). This is as expected since the clay binder bridging the FACs also serves as 'thermal bridges' among FAC particles (Fig. 10 (a)). This is also evidenced by the SEM images as shown in Fig. 9. The thermal conductivity of FAC-SSF is not sensitive to the FAC particle size, rather it is dictated most by the volume ratio between solid phases and air within the material. On the other hand, the mechanical properties (Young's modulus and strength) are controlled both by the clay content as well as the FAC particle size as previously discussed – i.e., the elastic modulus and strength increase as the clay content increases and smaller FACs (ES106) lead to higher mechanical performance due to higher particle strength and larger (accumulated) contact area among FACs, see Fig. 10 (c) and (d).

A comparison between the available foamed geopolymers (Huang et al., 2018; Liu et al., 2014; Samson et al., 2017; Zhang et al., 2015) and geopolymer with micro-size light weight fillers such as hollow glass bubbles (HGB) (Shao et al., 2018), polystyrene beads (Duan et al., 2017), and high-strength lightweight cementitious composites containing micro-size lightweight fillers previously studied by the authors (Brooks et al., 2018) indicates that the FAC synthetic foam produced in this study occupies a unique property space that has lower thermal conductivity than most of the structural lightweight materials with higher apparent density (>600 kg/m^3), while having significantly higher mechanical strength than low-density foamed concrete and geopolymer materials (compressive strength <4.5 MPa), see Fig. 11. Together with its low production costs and exceptional ability to endure high temperatures, the FAC synthetic foam produced is well suited for a wide variety of applications including refractory lining, fire- and weather-resistant building siding, as well as for the thermal insulation of industrial facilities, where both mechanical strength and thermal insulation property (low density) are desired. In addition, the inorganic FAC foam with low thermal conductivity and moderate mechanical strength can also be used as 'thermal breaks' at certain building locations – e.g., at the joint between foundation and structural framing in light frame structures and the interface between floor slab and exterior envelope in reinforced concrete buildings, to reduce thermal bridging (Totten et al., 2008).

4. Modeling thermal property of FAC-SSF

The total effective thermal conductivity (ETC) of fly-ash cenosphere synthetic solid foam (FAC-SSF) is attributed to three components: (1) heat conduction through the solid and the gas; (2) heat convection within the cells; and (3) heat radiation through the cell walls and across the cell voids (Schuetz and Glicksman, 1984). The contribution of heat convection is insignificant when the Grashof number (which describes the ratio of the buoyant force driving convection to the viscous force opposing it) is less than about 1000 (Gibson and Ashby, 1999). For foam having cell sizes less than 10 mm, this condition is generally satisfied, thus, the heat convection can be ignored for the small air cells within FAC-SSF.

Radiation may also contribute to the total ETC of synthetic foam materials, and the radiative thermal conductivity, χ^r, can be estimated by the unit cell method developed by Singh and Kaviany (1994) as:

$$\chi^r = 4F_E\sigma d_p\overline{T}^3 \tag{1}$$

where σ is the Stefan-Boltzmann constant; d_p is the particle diameter; $\overline{T}$ is the average temperature, and F_E is the radiation exchange factor that may be calculated as (Jia et al., 2018):

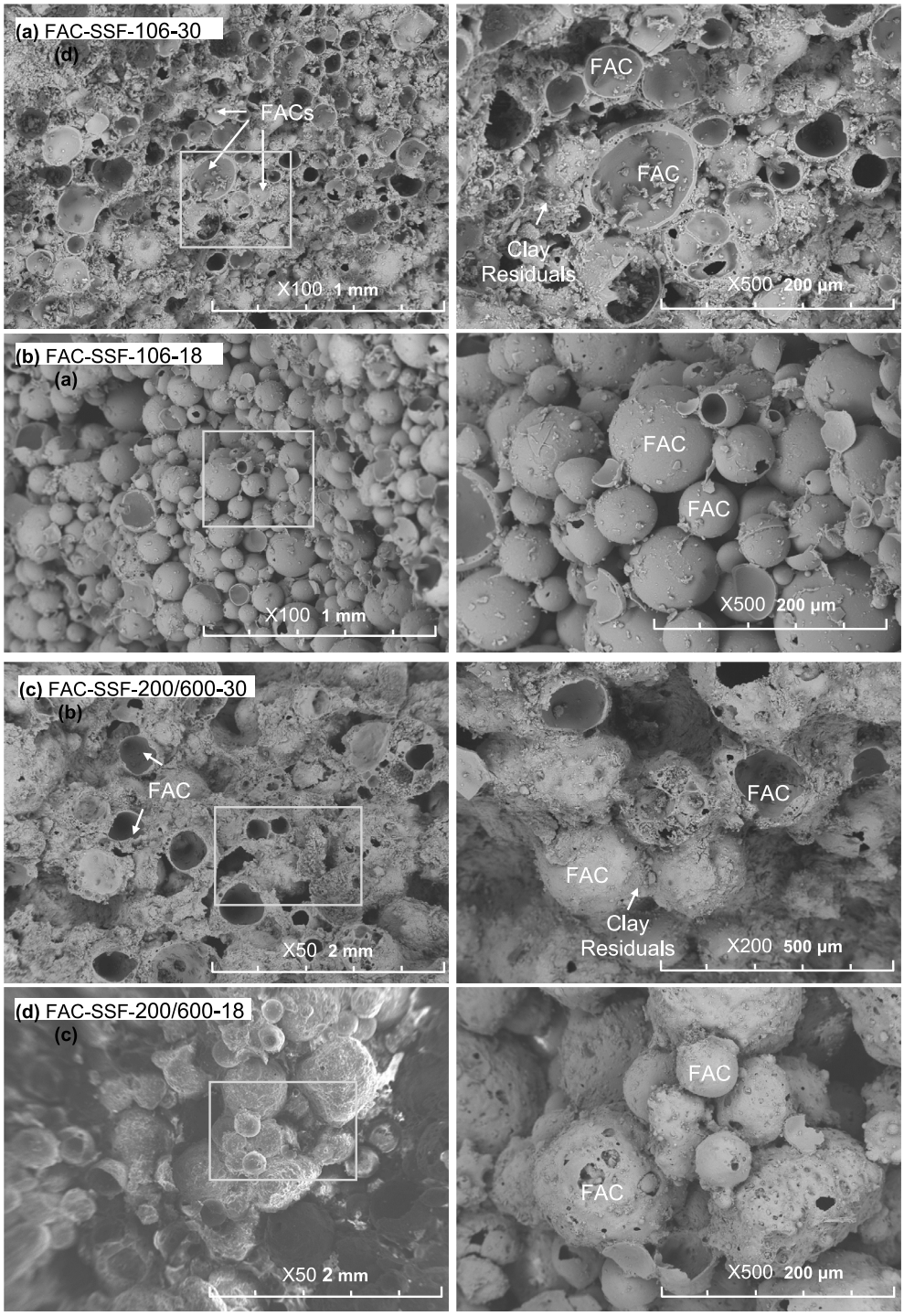

Fig. 9. SEM images showing the fractography of fly-ash cenosphere synthetic solid foams: (a) FAC–SSF–106-30 (high clay content); (b) FAC–SSF–106-18 (low clay content); (c) FAC–SSF–200/600–30; (d) FAC–SSF–200/600-18.

$$F_E = \frac{1}{1/\phi_{a,\mathrm{IP}} - 1} \tag{2}$$

where, $\phi_{a,\mathrm{IP}}$ is the volume fraction of air within the inter-particle void space as shown in Fig. 10 (a). For the FAC-SSF studied in this paper, $\phi_{a,\mathrm{IP}}$ is mostly in the range of 0.44–0.55, d_p is estimated as the medium particle size, D_{50} (81.3 µm and 349.1 µm for ES106 and ES200/600 FAC, respectively (see Table 1), and $\overline{T}$ is taken as room temperature (300 K). Therefore, the estimated radiative conductivities are in the range of 3.9×10^{-4} to 6.1×10^{-4} W/mK and 1.7×10^{-3} to 2.6×10^{-3} W/mK for ES106 and ES200/600 respectively. Since the contributions from both heat convection and radiation are relatively trivial as compared to conduction, the ETC of FAC-SSF is estimated based primarily on heat conduction.

The ETC of FAC-SSF from heat conduction is estimated via a three-step homogenization procedure as described in Fig. 12. In the first step, the thermal conductivity of hollow FAC particles is

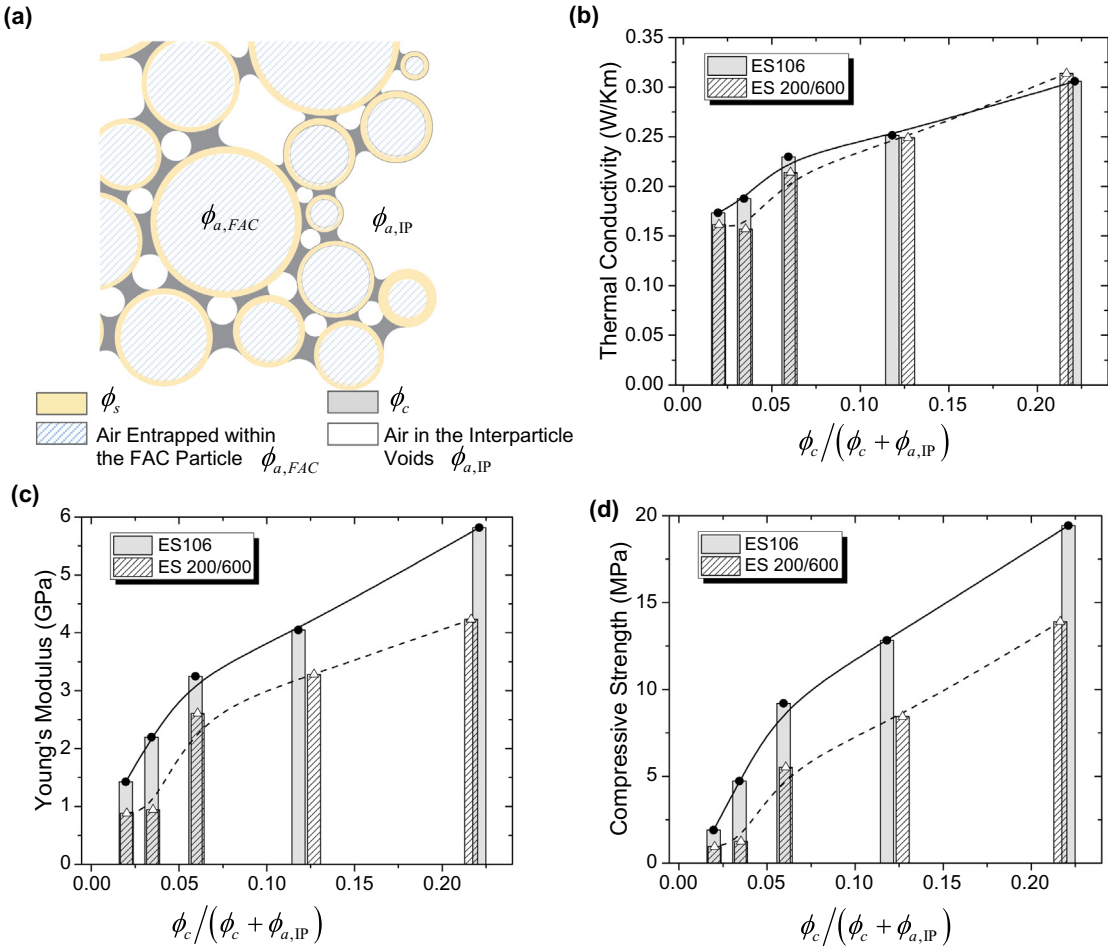

Fig. 10. Effects of FAC particle size and clay content, $\phi_c/(\phi_c+\phi_{a,\mathrm{IP}})$, on thermal and mechanical properties of FAC-SSF: (a) illustrative figure showing the clay content in the interparticle void space among FACs; and the change of (b) thermal conductivity, (c) Young's modulus; and (d) compressive strength.

equivalently represented by solid particles of the same size using the effective medium theory (EMT), see Fig. 12 (a); then, ETC of the FAC-clay system is obtained through differential effective medium theory (D-EMT), see Fig. 12 (b); lastly, the Eucken model (Eucken, 1932) is applied to calculate the final ETC of the FAC-SSF material with the consideration of porosity distribution and connectivity of the solid phases (Fig. 12 (c)).

In the first step, the equivalent thermal conductivity of a FAC particle is obtained by equaling the thermal conductivity of a hollow particle to an equivalent solid particle with the same size and shape, see Fig. 12 (a). For the i-th FAC particle, given the inner and outer radius r_1 and r_2, its equivalent TC, χ_i^{eq}, can be obtained through effective medium theory as (Jia et al., 2018; Nan, 1993):

$$\chi_i^{eq}=\frac{3+\left(\frac{\chi_a}{\chi_s}-1\right)(1+2f)}{3+\left(\frac{\chi_a}{\chi_s}-1\right)(1-f)}\chi_s \tag{3}$$

where χ_a and χ_s are the thermal conductivities of the air (core) and shell, respectively; and $f=(1+t_s/r_2)^{-3}$, $t_s=r_2-r_1$ is the thickness of the shell, see Fig. 12 (a). For the FAC used in this study, χ_a and χ_s are taken as 0.0257 W/mK and 2.0 W/mK, respectively.

Next, the ETC of polydispersed FAC-clay binder system, χ_{FAC-c}, is estimated using differential effective medium theory (D-EMT), where the equivalent FAC particles are homogenized into the FAC-clay binder system incrementally – for the addition of the i-th FAC particle, we have (Gao and Zhou, 2006):

$$\frac{d\chi_{FAC-c}}{d\phi_i}=\left(\frac{1}{1-\phi_i}\right)\frac{3\left(\chi_i^{eq}-\chi_{FAC-c}\right)\chi_{FAC-c}}{\left(\chi_i^{eq}+2\chi_{FAC-c}\right)},\qquad i=1,2,\ldots,N \tag{4}$$

where N is the total number of FAC particles with different sizes, ϕ_i is the volume fraction of the i-th FAC particle in the FAC-clay binder system, χ_{FAC-c} is the homogenized thermal conductivity of clay containing (i-1) FAC particles, and when $i=1$ $\chi_{FAC-c}=\chi_c$ where χ_c is the thermal conductivity of the clay binder.

Once the ETC of the FAC-clay system is obtained (Fig. 12 (b)), the ETC of the final FAC-SSF can be calculated using Eucken model (Eucken, 1932):

$$\overline{\chi}_{Eucken}=\chi_{FAC-c}\left(\frac{1+2\phi_{a,IP}(1-C)/(1+2C)}{1-\phi_{a,IP}(1-C)/(1+2C)}\right) \tag{5}$$

where $C=\chi_{FAC-c}/\chi_a$; and $\phi_{a,\mathrm{IP}}$ is the air volume fraction between FAC particles which does not include the air volume in the FAC inner cavity.

Fig. 13 compares the predicted ETCs as a function of the clay volume fraction in the interparticle void to the experimental data obtained for both ES106 and ES200/600 FAC-SSFs. The volume

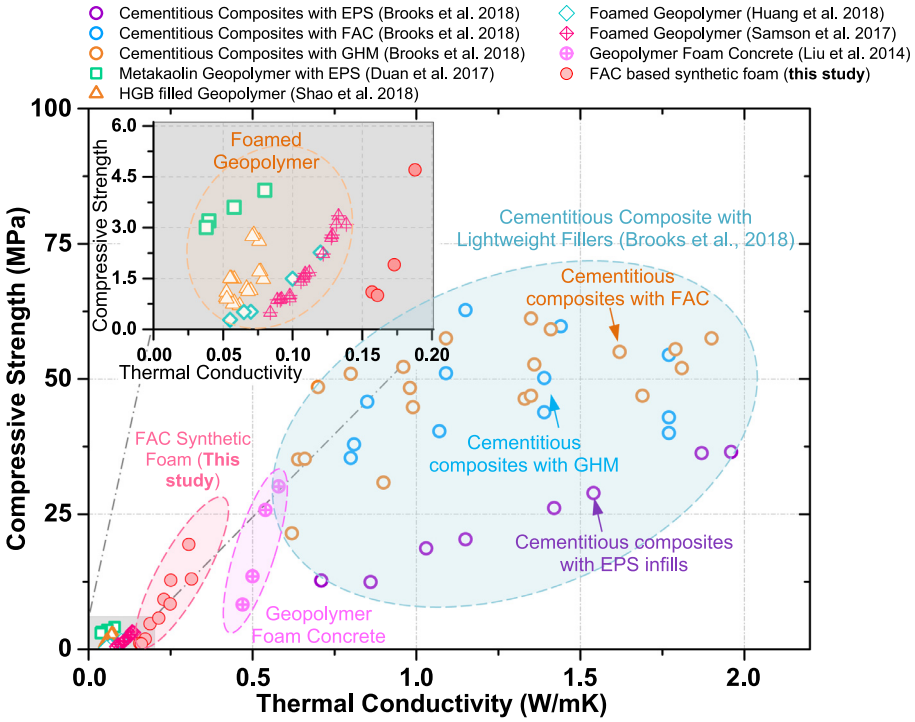

Fig. 11. Comparison of thermal and mechanical properties of the FAC-SSF developed herein with other inorganic lightweight insulating materials.

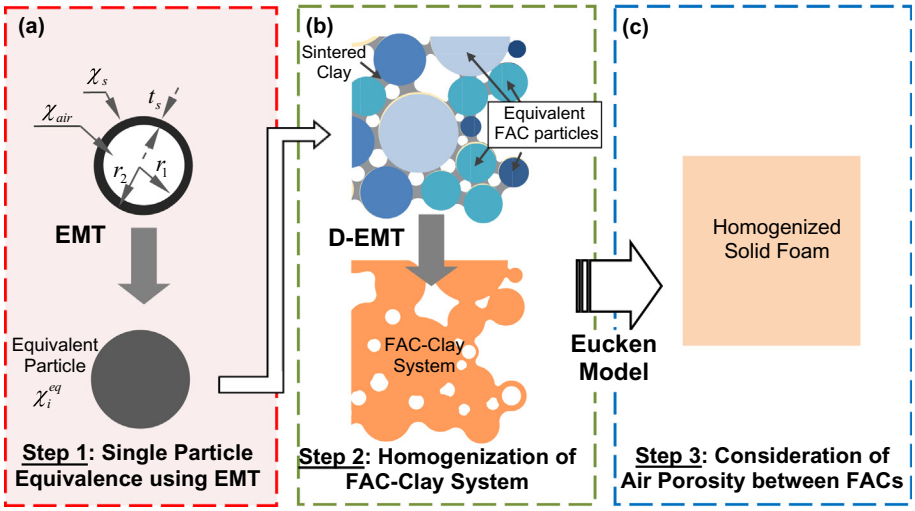

Fig. 12. A three-step homogenization procedure to obtain the effective thermal conductivity (ETC) for FAC-SSF.

fractions of each constituent were taken from the experimental values as listed in Table 2. The thermal conductivities of air, sintered clay, and FAC shell were taken as 0.0257 W/mK, 1.022 W/mK, and 2.0 W/mK, respectively. The yellow bands in Fig. 12 indicates the range of FAC packing density (i.e., 40–50%) since the FAC packing densities for the samples made in this study are mostly in this range, see Table 2. Overall, the ETCs predicted by the three-step homogenization procedure shown in Fig. 12 agree closely with the experimental data. However, it was noticed that the model tends to overestimate the ETC when the clay volume fraction is low and underestimates the ETC when the clay volume fraction is high, see Fig. 13. This is likely due to the increased 'thermal bridging' between FAC particles when clay content is higher – when clay content increases, more FAC particles are interconnected to form a shorter conduction path, thus, the thermal conductivity tested may become higher than the values predicted by the Eucken model which is based on self-consistent field theory (Eucken, 1932).

5. Conclusions

In this study, a novel inorganic solid foam material was developed from recycled fly ash cenospheres (FACs), where hollow FAC particles were minimally connected by clay binder materials. Mixing a low fraction of clay particles diluted in water enabled minimal contacts among the hollow FACs and was benefitted by a natural capillary-assisted effect to trap the binder materials at the

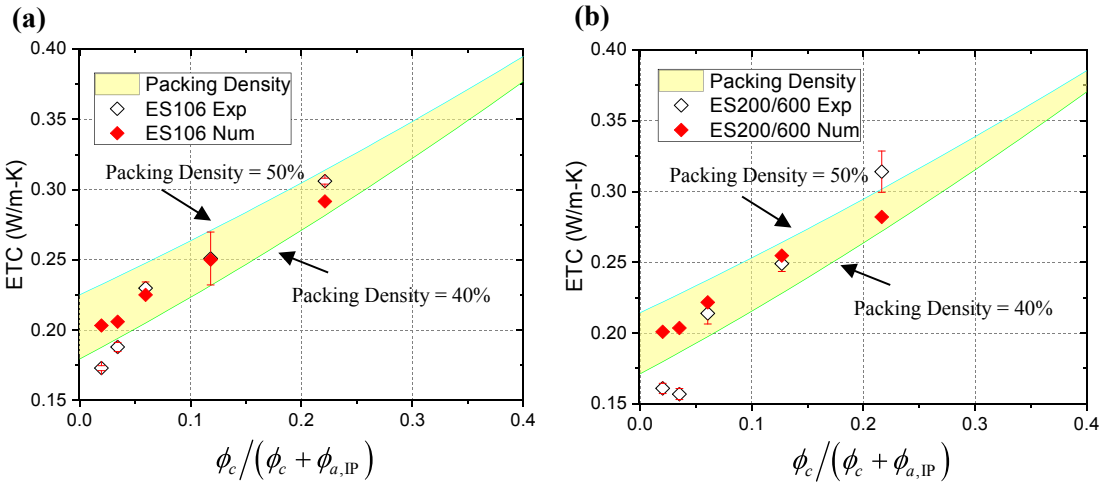

Fig. 13. Effective thermal conductivity of foams: (a) ES106 FAC-SSF; and (b) ES200/600 FAC-SSF.

FAC junction locations. The thermophysical and mechanical properties of the fly-ash cenosphere synthetic solid foam (FAC-SSF) were studied as functions of particle size and clay content in the interparticle void system. It was found that the thermal properties (thermal conductivity and volumetric heat capacity) are mostly functions of solids content (particle size has very little effect); whereas the mechanical properties (Young's modulus and strength) of FAC-SSF are dictated by both FAC particle size and the volume fraction of clay in the interparticle voids. The clay binder content also determines the fracture modes of FAC-SSF – i.e., as the clay binder content increases, the materials' failure mode transforms from the breakage of links between FAC particles to the breakage of FAC shells. This is also reflected in the initial failure modes of the compression test, where the split failure and shear failure are observed for the low and high clay binder content specimens. The inorganic synthetic foams developed have the potential for thermal insulation applications taking advantage of their relatively simple and scalable manufacturing process, minimal use of binder materials (saving clay for brick manufacturing), and relatively high mechanical strength and highly tailorable properties. A numerical method is proposed in this study to predict the effective thermal conductivity (ETC) of FAC-SSF under different thermal percolation paths. The comparison of simulated ETCs shows good agreements with experimental data.

Declaration of competing interest

None.

Acknowledgements

This research is partially sponsored by US National Science Foundation (NSF) (CMMI-1663302) and US Department of Energy (DE-EE-0008677). The funding supports from NSF and DOE are greatly appreciated. The views and opinions expressed in this article are those of the authors and do not necessarily reflect the point of funding agencies. The authors would like to thank Professor Jialai Wang and Mr. Yi Fang from University of Alabama for the help in microscopy imaging.

References

Barbhuiya, S.A., Gbagbo, J.K., Russell, M.I., Basheer, P.A.M., 2009. Properties of fly ash concrete modified with hydrated lime and silica fume. Constr. Build. Mater. 23, 3233–3239. https://doi.org/10.1016/j.conbuildmat.2009.06.001.

Bernal, S.A., Provis, J.L., 2014. Durability of alkali-activated materials: progress and perspectives. J. Am. Ceram. Soc. 97, 997–1008. https://doi.org/10.1111/jace.12831.

Biswas, K., Shrestha, S.S., Bhandari, M.S., Desjarlais, A.O., 2016. Insulation materials for commercial buildings in North America: an assessment of lifetime energy and environmental impacts. Energy Build. 112, 256–269. https://doi.org/10.1016/j.enbuild.2015.12.013.

Blissett, R.S., Rowson, N.A., 2012. A review of the multi-component utilisation of coal fly ash. Fuel 97, 1–23. https://doi.org/10.1016/j.fuel.2012.03.024.

Brooks, A.L., Zhou, H., Hanna, D., 2018. Comparative study of the mechanical and thermal properties of lightweight cementitious composites. Constr. Build. Mater. 159, 316–328. https://doi.org/10.1016/j.conbuildmat.2017.10.102.

Chen, F., Zhang, J., Li, N., Zhang, C., Ji, B., Hu, L., Zhao, T., Wang, Z., Zhang, S., 2018. Heat insulating, fire retardant and flexible inorganic nanocomposite paper. Mater. Des. 144, 281–289. https://doi.org/10.1016/j.matdes.2018.02.039.

Chindaprasirt, P., Homwuttiwong, S., Sirivivatnanon, V., 2004. Influence of fly ash fineness on strength, drying shrinkage and sulfate resistance of blended cement mortar. Cement Concr. Res. 34, 1087–1092. https://doi.org/10.1016/j.cemconres.2003.11.021.

Deepthi, M.V., Sharma, M., Sailaja, R.R.N., Anantha, P., Sampathkumaran, P., Seetharamu, S., 2010. Mechanical and thermal characteristics of high density polyethylene-fly ash Cenospheres composites. Mater. Des. 31, 2051–2060. https://doi.org/10.1016/j.matdes.2009.10.014.

Duan, P., Song, L., Yan, C., Ren, D., Li, Z., 2017. Novel thermal insulating and lightweight composites from metakaolin geopolymer and polystyrene particles. Ceram. Int. 43, 5115–5120. https://doi.org/10.1016/j.ceramint.2017.01.025.

Dwivedi, A., Jain, M.K., 2014. Fly ash – waste management and overview : a review. Recent Res. Sci. Technol. 6, 30–35.

Eucken, A., 1932. Thermal conductivity of ceramic refractory materials; calculation from thermal conductivity of constituents. Ceram. Abstr. 11 https://doi.org/10.1007/s10853-006-7637-x.

Fomenko, E., Anshits, N., Pankova, M., 2011. Fly ash cenospheres: composition, morphology, structure, and helium permeability. In: World of Coal Ash Conference (Denver, CO, USA).

Gao, L., Zhou, X.F., 2006. Differential effective medium theory for thermal conductivity in nanofluids. Phys. Lett. Sect. A Gen. At. Solid State Phys. 348, 355–360. https://doi.org/10.1016/j.physleta.2005.08.069.

Gibson, L.J., Ashby, M.F., 1999. Cellular Solids: Structure and Properties. Cambridge University Press.

Gustafsson, S.E., 1991. Transient diffusivity plane source techniques for thermal conductivity measurements of solid materials and thermal. Rev. Sci. Instrum. 62, 797–804.

Hanif, A., Lu, Z., Li, Z., 2017. Utilization of fly ash cenosphere as lightweight filler in cement-based composites – a review. Constr. Build. Mater. 144, 373–384. https://doi.org/10.1016/j.conbuildmat.2017.03.188.

He, Y., 2005. Rapid thermal conductivity measurement with a hot disk sensor: Part 1. Theoretical considerations. Thermochim. Acta 436, 122–129. https://doi.org/10.1016/j.tca.2005.06.026.

Huang, Y., Gong, L., Shi, L., Cao, W., Pan, Y., Cheng, X., 2018. Experimental investigation on the influencing factors of preparing porous fly ash-based geopolymer for insulation material. Energy Build. 168, 9–18. https://doi.org/10.1016/j.enbuild.2018.02.043.

ISO22007-2:2008, 2008. Plastics - Determination of Thermal Conductivity and Thermal Diffusivity - Part 2: Transient Plane Source Method.

Jia, Z., Wang, Z., Hwang, D., Wang, L., 2018. Prediction of the effective thermal conductivity of hollow sphere foams. ACS Appl. Energy Mater. 1, 1146–1157.

https://doi.org/10.1021/acsaem.7b00264.
Lam, L., Wong, Y.L., Poon, C.S., 2000. Degree of hydration and gel/space ratio of high-volume fly ash/cement systems. Cement Concr. Res. 30, 747–756. https://doi.org/10.1016/S0008-8846(00)00213-1.
Liu, M.Y.J., Alengaram, U.J., Jumaat, M.Z., Mo, K.H., 2014. Evaluation of thermal conductivity, mechanical and transport properties of lightweight aggregate foamed geopolymer concrete. Energy Build. 72, 238–245. https://doi.org/10.1016/j.enbuild.2013.12.029.
McConville, C.J., Lee, W.E., 2005. Microstructural development on firing illite and smectite clays compared with that in kaolinite. J. Am. Ceram. Soc. 88, 2267–2276. https://doi.org/10.1111/j.1551-2916.2005.00390.x.
Miskin, M.Z., Jaeger, H.M., 2012. Droplet formation and scaling in dense suspensions. In: Proceedings of the National Academy of Sciences, pp. 4389–4394.
Nan, C.W., 1993. Physics of inhomogeneous inorganic materials. Prog. Mater. Sci. 37, 1–116. https://doi.org/10.1016/0079-6425(93)90004-5.
Ranjbar, N., Kuenzel, C., 2017. Cenospheres: a review. Fuel 207, 1–12. https://doi.org/10.1016/j.fuel.2017.06.059.
Rohatgi, P.K., Gupta, N., Schultz, B.F., Luong, D.D., 2011. The synthesis, compressive properties, and applications of metal matrix syntactic foams. JOM (J. Occup. Med.) 63, 36–42. https://doi.org/10.1007/s11837-011-0026-1.
Sadik, C., Amrani, I. El, Albizane, A., 2014. Recent advances in silica-alumina refractory : a review. J. Asian Ceram. Soc. 2, 83–96. https://doi.org/10.1016/j.jascer.2014.03.001.
Samson, G., Cyr, M., Gao, X.X., 2017. Thermomechanical performance of blended metakaolin-GGBS alkali-activated foam concrete. Constr. Build. Mater. 157, 982–993. https://doi.org/10.1016/j.conbuildmat.2017.09.146.
Schuetz, M.A., Glicksman, L.R., 1984. A basic study of heat transfer through foam insulation. J. Cell. Plast. 20, 114–121. https://doi.org/10.1177/0021955X8402000203.
Shao, N. ning, Zhang, Y. bo, Liu, Z., Wang, D. min, Zhang, Z. tai, 2018. Fabrication of hollow microspheres filled fly ash based foam geopolymers with ultra-low thermal conductivity and relative high strength. Constr. Build. Mater. 185, 567–573. https://doi.org/10.1016/j.conbuildmat.2018.07.077.
Sheikh, V., 2018. Limited availability of cementitious materials could impact the value chain. Amercian Coal Ash Assoc 34–36.
Siddique, R., 2010. Utilization of coal combustion by-products in sustainable construction materials. Resour. Conserv. Recycl. 54, 1060–1066. https://doi.org/10.1016/j.resconrec.2010.06.011.
Singh, B.P., Kaviany, M., 1994. Effect of solid conductivity on radiative heat transfer in packed beds. Int. J. Heat Mass Transf. 37, 2579–2583. https://doi.org/10.1016/0017-9310(94)90295-X.
Totten, P.E., O'Brien, S.M., Pazera, M., 2008. The effects of thermal bridging at interface conditions. In: Building Enclosure Science and Technology (BEST 1) Conference, p. 12. Minneapolis, MN.
Wi, S., Yang, S., Berardi, U., Kim, S., 2019. Assessment of recycled ceramic-based inorganic insulation for improving energy efficiency and flame retardancy of buildings. Environ. Int. 130, 104900. https://doi.org/10.1016/j.envint.2019.06.010.
Zhang, Z., Provis, J.L., Reid, A., Wang, H., 2015. Mechanical, thermal insulation, thermal resistance and acoustic absorption properties of geopolymer foam concrete. Cement Concr. Compos. 62, 97–105. https://doi.org/10.1016/j.cemconcomp.2015.03.013.
Zhou, H., Brooks, A.L., 2019. Thermal and mechanical properties of structural lightweight concrete containing lightweight aggregates and fly-ash cenospheres. Constr. Build. Mater. 198, 512–526. https://doi.org/10.1016/j.conbuildmat.2018.11.074.
Zyrkowski, M., Neto, R.C., Santos, L.F., Witkowski, K., 2016. Characterization of fly-ash cenospheres from coal-fired power plant unit. Fuel 174, 49–53. https://doi.org/10.1016/j.fuel.2016.01.061.